ACS Catalysis

pubs.acs.org/acscatalysis
Research Article

Reaction Pathways of Methanol Formation in CO_2 Hydrogenation over Pd-Based Catalysts

Denis Makhmutov, Elizaveta Fedorova, Anna Zanina, Christoph Kubis, Dan Zhao, Dmitry Doronkin, Nils Rockstroh, Stephan Bartling, Udo Armbruster, Sebastian Wohlrab,* and Evgenii V. Kondratenko*

Cite This: ACS Catal. 2025, 15, 2328−2341
Read Online

ACCESS | Metrics & More | Article Recommendations | Supporting Information

ABSTRACT: The production of methanol (CH_3OH) from CO_2 is an attractive solution for closing the carbon cycle and thus addressing both environmental concerns and raw material changes in the chemical industry. CuZn-based catalysts are the most intensively investigated materials in this regard but suffer from CH_3OH decomposition to CO with increasing CO_2 conversion. Pd-containing materials also show promising performance, but they are less understood from a mechanistic point of view. To bridge this gap, a series of catalysts based on CeO_2, ZrO_2, $Ce_{0.8}Zr_{0.2}O_2$, or CeO_2−SiO_2 supports with Pd or CuZnPd as active components were prepared. Comprehensive kinetic tests revealed that the catalysts containing only Pd species convert CO_2 to CO exclusively, followed by the hydrogenation of CO to CH_3OH. Using a feed consisting of CO and H_2, 100% CH_3OH selectivity was achieved. The role of Pd is to convert CO_2 to CO and to generate surface species from H_2, which are involved in the hydrogenation of CO to CH_3OH probably on the surface of support. In situ Fourier transform infrared spectroscopy tests have identified $HCOO^-$ species formed from gas-phase CO as surface precursors of CH_3OH. In contrast to the Pd/support catalysts, their CuZnPd/support counterparts convert CO_2 directly into CH_3OH in parallel with CO. These differences were explained by structural/electronic changes in Pd due to alloying with Cu as revealed by in situ X-ray photoelectron and X-ray absorption spectroscopy. Overall, this study enhances understanding of the mechanistic aspects of product formation in the course of CO_2 hydrogenation to CH_3OH and highlights the significance of steady-state catalytic tests at different space velocities to identify primary and secondary pathways, offering valuable insights for the tailored design of efficient catalysts for CH_3OH production from CO_2.

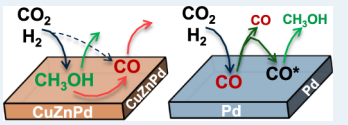

KEYWORDS: *CO_2 hydrogenation, methanol synthesis, Pd catalysts, reaction mechanism, DRIFTS, XANES, kinetic analysis*

1. INTRODUCTION

Growing concerns about carbon dioxide (CO_2) emissions and their pivotal role in global climate change have intensified the search for sustainable approaches to mitigate the environmental impact of this greenhouse gas.[1,2] Among various strategies, hydrogenation of CO_2 to methanol has emerged as a particularly promising route.[3−6] This chemical is used as a clean energy carrier, as a storage medium for hydrogen in a circular economy, and as a building block in many industrial processes.[7−9] It is currently produced using synthesis gas, a mixture of carbon monoxide and hydrogen, generated by strongly endothermic steam reforming of methane resulting in high CO_2 emissions.[9−11] CO_2 is added to the methanol synthesis feed to increase catalyst productivity.[12−14] Copper-based catalysts are widely used for the production of methanol,[15,16] with a mixed metal oxide $CuZnAlO_x$ being the most common catalyst composition.[17−19] However, it has shortcomings such as suboptimal methanol yield and significant activity for CO formation via the reverse water gas shift (RWGS) reaction and due to methanol decomposition to CO.[18,20−22] Consequently, there has been considerable research aimed at modifying conventional CuZn-based catalysts by incorporating various metal oxides such as ZrO_2, CeO_2, and others.[23−27] These promoters are believed to modulate catalyst properties with the purpose of enhancing CO_2 adsorption by creating basic sites, improving the dispersion of surface Cu^0 sites, or enhancing hydrothermal stability.[16,17,28]

The catalytic activity of Cu-based catalysts can be further enhanced by promoting them with Pd.[29,30] This promoter can effectively activate hydrogen[31] and spillover adsorbed species to reduce CuO_x and to hinder reoxidation of the resulting Cu^0 species.[32] Jiang et al.[33] have reported on a strong synergistic effect between Pd and Cu on the rate of methanol formation over a Pd(0.34)-Cu/SiO_2 catalyst. The rate obtained was twice as high as the sum of the rates determined over the Cu- or Pd-containing counterparts. This effect was attributed to the formation of nanosized Pd−Cu alloy particles, which affect the formation of surface hydrogen species and their reactivity. Choi et al.[30] explained higher CO_2 conversion and methanol productivity over Pd-promoted Cu/CeO_2 catalysts compared

Received: December 3, 2024
Revised: January 2, 2025
Accepted: January 13, 2025

to their Pd-free counterparts due to higher dispersion and surface concentration of Cu^0.

Pd-based catalysts without Cu are also attractive for CO_2 hydrogenation due to their favorable activity and high selectivity to methanol.[34−36] Fan et al. studied the unpromoted Pd/CeO_2 catalyst[37] at 230 °C and a total pressure of 30 bar. The methanol selectivity of 91.7% at 3.1% CO_2 conversion was obtained, and no catalyst deactivation was observed during 80 h on stream. Similar to Cu-based catalysts, the addition of ZnO or using ZnO as a support can enhance the activity and methanol selectivity of Pd-based catalysts. The improvement is typically related to the presence of a Pd−Zn alloy, which readily forms atomic hydrogen from gas-phase H_2 and shows high resistance to sintering.[38−41] Bahruji et al.[42] reported 60% methanol selectivity at 10.7% CO_2 conversion over Pd/ZnO catalysts at 250 °C and 20 bar. The formation of PdZn alloy nanoparticles with a specific particle size and surface structure was identified as the key factor affecting methanol production. Malik et al.[43] also concluded that the presence of well-dispersed and uniformly distributed nanoparticles of Pd or PdZn is crucial for methanol formation. A nearly 100% selectivity to methanol at 7.7% CO_2 conversion was achieved over the Ca-doped $PdZn/CeO_2$ catalyst at 220 °C and 30 bar.

It is also worth mentioning that Cu-based catalysts are able to decompose CH_3OH to CO and H_2 in the course of CO_2 hydrogenation.[17,18,22,44] This is reflected by a decrease in CH_3OH selectivity and, conversely, an increase in CO selectivity as CO_2 conversion increases. In contrast, numerous Pd-based catalysts demonstrate high methanol selectivity at high degrees of CO_2 conversion.[42,43] Is this due to a hindered activity of these materials to decompose methanol? Does the reaction scheme of product formation depend on the kind of active component, i.e., Cu, Pd or CuPd alloy? The answers to these questions would certainly contribute to targeted design of selective catalysts for CO_2 hydrogenation to CH_3OH.

Thus, the main objective of the present study was to elucidate the reaction pathway(s) leading to CO and CH_3OH in CO_2 hydrogenation over Pd-based catalysts in comparison to the $CuZnO_x$-containing catalysts. In pursuit of this goal, sophisticated kinetic tests were performed at different temperatures and contact times using reaction feeds with different ratios of CO/CO_2. The obtained selectivity-conversion relationships for CO and CH_3OH were used to determine primary and secondary reaction pathways and to understand their interplay. In situ DRIFTS experiments were instrumental in identifying the intermediates/adsorbed species responsible for product formation and thus distinguishing the differences between Pd/support and CuZnPd/support catalysts in terms of methanol formation. Using scanning transmission electron microscopy (STEM) coupled with energy-dispersive X-ray spectroscopy (EDX), X-ray absorption near-edge structure (XANES), and extended X-ray absorption fine structure (EXAFS) spectra enabled the elucidation of the morphology and distribution of the elements, as well as their oxidation and alloying states in the catalysts.

2. MATERIALS AND METHODS

2.1. Catalyst Preparation. For the preparation of CeO_2, $Ce(NO_3)_3{\cdot}6H_2O$ (Sigma-Aldrich, 99%) was pulverized and calcined at 400 °C with a heating rate of 5 $K{\cdot}min^{-1}$ for 4 h. For the synthesis of CeO_2-SiO_2 (30:70), the $Ce(NO_3)_3{\cdot}6H_2O$ was mixed with SiO_2 (Fluka, 99%) at room temperature. The resulting mixture was placed in a drying oven, heated to 150 °C with a heating rate of 2 $K{\cdot}min^{-1}$, and stirred every 5 min for 1 h. This procedure was repeated until the cerium nitrate had melted and been absorbed by SiO_2. The temperature was then increased to 200 °C with a heating rate of 2 $K{\cdot}min^{-1}$ and held for 4 h. Finally, the precursor was calcined at 400 °C with a heating rate of 5 $K{\cdot}min^{-1}$ and held for another 4 h. The $Ce_{0.8}Zr_{0.2}O_2$ support was synthesized by dissolving $Ce(NO_3)_3{\cdot}6H_2O$ and $ZrO(NO_3)_2{\cdot}xH_2O$ (Sigma-Aldrich, 99%) in water under continuous stirring. After complete dissolution, citric acid was added to the solution and the resulting support precursor was stirred at room temperature for 1 h. Subsequently, the solvent was removed at 40 °C using a rotary evaporator and the remaining material was dried at 80 °C overnight. The resulting dried precursor was further pulverized and calcined at 400 °C with a heating rate of 5 $K{\cdot}min^{-1}$ and held at this temperature for 4 h.

The supported Pd- or CuZnPd-containing catalysts based on the support materials CeO_2, $Ce_{0.8}Zr_{0.2}O_2$, CeO_2-SiO_2 (30:70) and ZrO_2 (provided by Daiichi Kigenso Kagaku Kogyu Co. Ltd., Japan) were synthesized using the incipient wetness impregnation method. $Cu(NO_3)_2{\cdot}3H_2O$ (Roth, 98%), $Zn(NO_3)_2{\cdot}6H_2O$ (Sigma-Aldrich, 98%), and $Pd(NO_3)_2{\cdot}xH_2O$ (Alfa Aesar, 99.8%) were used as the sources of Cu, Zn, and Pd, respectively. Their corresponding content is 5, 2.5, and 1 wt %. For the synthesis of the CuZnPd/support catalysts, $Cu(NO_3)_2{\cdot}3H_2O$, $Zn(NO_3)_2{\cdot}6H_2O$, and $Pd(NO_3)_2{\cdot}xH_2O$ were dissolved in deionized water. For the Pd/support catalysts, only $Pd(NO_3)_2{\cdot}xH_2O$ was dissolved in deionized water. After complete dissolution, the solutions were added dropwise to the supports. The resulting solids were dried at 80 °C for 3 h and then calcined at 400 °C for 4 h with a heating rate of 5 $K{\cdot}min^{-1}$. All prepared catalysts were sieved to give particles of 310−715 μm. To simplify the description of the catalyst composition, the resulting catalysts 1 wt %Pd/CeO_2, 1 wt %Pd/ZrO_2, 1 wt %$Pd/Ce_{0.8}Zr_{0.2}O_2$, 1 wt %Pd/CeO_2-SiO_2 (30:70), 5 wt %Cu2.5 wt %Zn1 wt %Pd/ZrO_2, 5 wt %Cu2.5 wt %Zn1 wt %$Pd/Ce_{0.8}Zr_{0.2}O_2$, and 5 wt %Cu2.5 wt %Zn1 wt %Pd/CeO_2-SiO_2 (30:70) are referred to as Pd−Ce, Pd−Zr, Pd-CeZr, Pd-CeSi, CuZnPd-Zr, CuZnPd-CeZr, CuZnPd-CeSi, respectively.

2.2. Catalyst Characterization. Powder X-ray diffraction (PXRD) measurements were conducted using an X'Pert Pro diffractometer (Panalytical) with CuKα radiation (λ = 1.5418 Å, 40 kV, 40 mA) and an X'Celerator RTMS detector.

Elemental analysis of the catalysts was performed by inductively coupled plasma optical emission spectroscopy (ICP-OES) using an Agilent 715 ES spectrometer.

The surface area (S_{BET}) of the catalysts was determined by conducting N_2 physisorption experiments at −196 °C. Prior to the measurements, catalyst samples were pretreated in vacuum at 250 °C for 2 h to remove the adsorbed water. The desorption isotherms were analyzed using the BET method. The Belsorp mini II setup from Bel Japan was used for this analysis.

The reducibility of the catalysts was determined by temperature-programmed reduction (H_2-TPR) tests using an in-house developed setup equipped with 8 individually heated continuous-flow fixed-bed quartz reactors. Prior to measurements, samples (50 mg) were pretreated at 300 °C in an air flow (8 $mL{\cdot}min^{-1}$ per reactor) for 1 h, followed by cooling to room temperature in an Ar flow (10 $mL{\cdot}min^{-1}$) for 2 h. The treated catalysts were then individually heated to 700 °C with a heating rate of 10 $K{\cdot}min^{-1}$ in a 5 vol %H_2/Ar flow (10 mL·

https://doi.org/10.1021/acscatal.4c07462
ACS Catal. 2025, 15, 2328−2341

min^{-1}). H_2 and Ar were detected at the reactor outlet by an online mass spectrometer (Pfeiffer Vacuum OmniStar GSD 320) at m/z 2 and 40, respectively.

The basic properties of the catalysts were studied by temperature-programmed desorption measurements with CO_2 (CO_2-TPD) in the same setup as for H_2-TPR tests. Fresh catalyst samples (50 mg) were initially heated to 300 °C in a 5 vol %H_2/Ar flow (10 mL·min^{-1}) and kept at this temperature for 4 h. After reduction, the treated materials were cooled to 50 °C in Ar (10 mL·min^{-1}) and then exposed to the flow of 20 vol %CO_2/Ar (10 mL·min^{-1}) for 1.5 h at the same temperature. To remove physically adsorbed CO_2, the catalysts were flushed with Ar (10 mL·min^{-1}) at 50 °C for 3 h. Finally, they were individually heated to 700 °C with a rate of 10 K·min^{-1} in Ar (10 mL·min^{-1}). CO_2 (m/z 44) and Ar (m/z 40) were detected at the reactor outlet by the online mass spectrometer.

Scanning Transmission Electron Microscopy (STEM) tests were performed utilizing a probe aberration-corrected JEM-ARM200F (JEOL, Corrector: CEOS) at an operating voltage of 200 kV. The microscope is equipped with a JED-2300 (JEOL) energy-dispersive X-ray (EDX) spectrometer, which employs a silicon drift detector (dry SD60GV). A High-Angle Annular Dark Field (HAADF) detector and an Annular Bright Field (ABF) detector were used for imaging. The solid samples were deposited onto a holey carbon-supported Cu grid (mesh 300, Pd−Zr) or Ni grid (mesh 300, CuZnPd-Zr) without any pretreatment and subsequently transferred to the microscope for imaging and analysis.

Pseudo in situ X-ray photoelectron spectroscopy (XPS) measurements were performed in a laboratory Near Ambient Pressure X-ray photoelectron spectroscopy system (NAP-XPS, SPECS Surface Nano Analysis GmbH, Germany). The setup is equipped with a differentially pumped Phoibos 150 electron energy analyzer and a monochromated Al Kα radiation source (E = 1486.6 eV) operated at 70 W and 15 kV. The system is connected to a High-Pressure Cell (HPC 20, SPECS Surface Nano Analysis GmbH, Germany) which offers sample heating by a halogen lamp (up to 800 °C) and is equipped with 4 mass flow controllers (Bronkhorst) at the gas inlet and a manual back pressure regulator (Swagelok, USA) at the outlet. For the current experiments at a total pressure of 10 bar, a flow of 20 mL·min^{-1} H_2 and 20 mL·min^{-1} N_2 for reduction and 5 mL·min^{-1} CO_2, 15 mL·min^{-1} H_2 and 20 mL·min^{-1} N_2 flows as in CO_2 hydrogenation tests were used for the catalyst treatment. The sample is heated to 300 °C (reduction) or 200 °C (reaction) in 50 vol % H_2/N_2 with 5 K·min^{-1}. After a given time on stream, the sample was cooled down in N_2 before the cell was evacuated and the sample could be transferred under vacuum to the measurement chamber. The powder samples are pressed on a stainless-steel sample plate using a laboratory press with a 5 mm diameter and a load of about 1 t. Temperature is monitored by a thermocouple on the sample plate pressed to the sample surface. The electron binding energies are referenced to the C 1s core level of carbon at 284.8 eV (C−C and C−H bonds). For analysis, the peaks were deconvolved with Gaussian−Lorentzian curves using the software Unifit 2023.

X-ray absorption near-edge structure (XANES) and extended X-ray absorption fine structure (EXAFS) spectra at the Pd, Zn, and Cu K edges were recorded at the P65 beamline of the PETRA III synchrotron (DESY, Hamburg) in fluorescence mode using a silicon drift detector (Hitachi Vortex-ME4, 2 mm detector thickness). The energies of the X-ray photons were selected by the Si(111) and Si(311) double-crystal monochromator for Zn and Cu, and Pd, respectively. The beam size was set by means of slits to a dimension of 0.3 (vertical) × 1.5 (horizontal) mm^2. The spectra were normalized and the background of EXAFS was subtracted by using the Athena program from the IFEFFIT and Demeter packages.[45] The interatomic distances (r), energy shift (δE_0), coordination numbers (CN), and mean-square deviation of interatomic distances (σ^2) were refined during the fitting of k^1, k^2, and k^3-weighted data in R-space. The amplitude reduction factors (S_0^2) used for the fits were obtained by fitting spectra of the corresponding metal foils. The absolute misfit between the theory and the experiment is expressed by ρ. To monitor the structural changes of Pd−Zr and CuZnPd-Zr under reaction conditions, in situ XAS measurements were performed at the Pd, Zn, and Cu K edges. In summary, approximately 10 mg of the catalyst (sieve fraction: 100−200 μm) was placed between two layers of quartz wool within a quartz capillary (inner diameter: 1 mm, wall thickness: 0.02 mm, WJM Glas). The catalyst was heated up to 300 °C in He (15 mL·min^{-1}) with a temperature ramp of 5 K·min^{-1} by means of a Leister LE mini kit hot air blower. Once the temperature was stabilized at 300 °C, the catalyst was exposed to 50 vol % H_2 in He (15 mL·min^{-1}) for 40 min for reduction. After cooling to 200 °C in the aforementioned atmosphere, a CO/H_2 (1:3 ratio, 16 mL·min^{-1} total flow) was introduced to the capillary at 20 bar. The reaction time was maintained for 1 h, and the measurements were conducted separately, each time with a new catalyst batch for the Cu and Zn K edges (in a single scan) and for the Pd K edge. EXAFS was analyzed on the spectra measured in the last 7 min of each respective step for the Cu K edge, while data averaged over the whole 1 h (to enhance the signal-to-noise ratio, given that no notable changes occurred during each step) was employed to analyze the Pd K edge spectra.

In-situ DRIFTS experiments were performed using a Nicolet iS10 FTIR spectrometer equipped with a high-pressure high-temperature reaction cell (Harrick) with ZnSe windows. The cell functioned as a fixed-bed continuous-flow reactor and contained approximately 60 mg of each catalyst. The samples were initially pretreated at 300 °C and 20 bar in a flow of 50 vol %H_2/He (50 mL·min^{-1}) for 2 h, followed by a 1 h He feed (50 mL·min^{-1}) for hydrogen removal. The catalysts were subsequently cooled to 200 °C under the same gas flow conditions, while recording the background spectrum. To study CO_2 and CO adsorption, the catalysts were exposed to 22 vol %CO_2/He and 5 vol %CO/He with a total gas flow rate of 45 mL·min^{-1} for 1 h. In order to investigate the transformations of adsorbates formed after CO_2 exposure, the samples were treated in 50 vol %H_2/He (50 mL·min^{-1}) for 2 h. To remove all adsorbates from the surface, the samples were heated to 300 °C in 50 vol %H_2/He (50 mL·min^{-1}) for 1 h. DRIFTS experiments were also performed using a relevant reaction gas mixture of 22 vol %CO_2/66 vol %H_2/He with a total gas flow rate of 45 mL·min^{-1} at 20 bar for 2 h. Hereafter, the catalysts were exposed to He (50 mL·min^{-1}) to remove gas-phase products and feed components.

2.3. Catalytic Experiments. CO_2 hydrogenation to methanol at 20 bar was studied in an in-house built setup comprising 51 continuous-flow fixed-bed stainless-steel tubular reactors operating in parallel. The total feed flow was evenly distributed using flow restrictors to maintain a constant flow in each reactor. The outlet gas from each reactor was directed

https://doi.org/10.1021/acscatal.4c07462
ACS Catal. 2025, 15, 2328−2341

sequentially for gas-chromatographic analysis using multiport valves. An online Agilent 7890A gas chromatograph (GC) was used to analyze the composition of the feed components and gaseous products. HP PlotQ and MolSieve 5A columns with a thermal conductivity detector (TCD) were utilized to separate CO, CO_2, H_2O, H_2, and N_2, while AL/S and FFAP columns with a flame ionization detector (FID) were employed to separate C_1−C_8 hydrocarbons, and methanol, dimethyl ether, methyl formate, respectively. To prevent condensation of high-boiling hydrocarbons, the stainless-steel lines between the reactor outlet and the online GC inlet were heated to 180 °C. Catalyst amounts ranging from 100 to 500 mg (315−710 μm) and feed flows varying from 4 to 21 mL·min^{-1} were used to achieve reciprocal modified contact time ($\tau_{modified}$, volumetric flow rate of feed per hour divided by the mass of the catalyst sample) values ranging from 700 to 12400 mL·g_{cat}^{-1}·h^{-1}. A layer of SiC (500−700 μm) atop the catalyst bed ensured preheating and plug flow of the top-supplied feed. Catalysts were pretreated in a 50 vol %H_2/N_2 flow (10 mL·min^{-1} per reactor) at 300 °C and 20 bar for 4 h before testing. The reaction was conducted with a feed of $CO_2/H_2/N_2$ = 1/3/4 or 3/9/1, corresponding to 12.5/37.5/50 and 23.1/69.3/7.6 vol %, respectively.

Catalytic tests were also performed at 50 bar in a high-pressure setup using a single stainless steel fixed-bed continuous-flow reactor filled with 3 g of each catalyst. Catalyst particles (315−710 μm) were loaded into the reactor and layered between quartz wool and quartz particles to preheat the feed gases and ensure plug flow. Catalyst pretreatment involved a stepwise increase in H_2 content from 0 to 100 vol % in a H_2/N_2 flow (33 mL·min^{-1}) at 300 °C and 6 bar total pressure over a 15 h program. This approach was selected to prevent the formation of hot spots in the catalyst layer, which could otherwise damage the catalyst structure during the reduction. The feed gas flow was varied from 90 to 300 mL·min^{-1} to achieve $\tau_{modified}$ values between 1800 and 6000 mL·g_{cat}^{-1}·h^{-1}. Unless otherwise specified, the gas mixture was composed of CO_2, H_2, and N_2 in a 1/3/4 ratio (12.5/37.5/50 vol %, respectively). The feed and product gases were analyzed using a Shimadzu GC-2010 Plus online gas chromatograph, equipped with HP PlotQ and MolSieve 5A columns connected to TCD, and HP PlotQ column connected to FID for component separation (CO, CO_2, H_2, N_2, C_1−C_4 alcohols, C_1−C_7 hydrocarbons, dimethyl ether, and methyl formate). To prevent product condensation, the reactor and pressurized lines were embedded in an oven at 150 °C, and the line between the backpressure regulator and the GC was heated to 100 °C. The feed gas concentration was determined through bypass measurements before and after catalytic experiments. In the experiments conducted to investigate the impact of adding CO to the feed gas, the reaction temperature and pressure were kept constant at 200 °C and 50 bar, respectively. The catalyst mass was 3 g, and the gas flow varied between 90 and 300 mL·min^{-1} for each feed gas composition. The gas mixture used in the feed consisted of CO, CO_2, H_2 and N_2 in the ratio x/1-x/3/4 (x/12.5-x/37.5/50 vol %, respectively), where x is the fraction of CO and varies between 0 and 1 (or in other terms 0 and 12.5 vol %).

In the experiments without added CO, the CO_2 conversion, product selectivity, and rates of CO_2 conversion to a certain reaction product were calculated according to the equations below:

$$X(CO_2) = \frac{\sum_i \nu_i \times x_i}{x_{CO_2}^{out} + \sum_i \nu_i \times x_i} \quad (1)$$

$$S(i) = \frac{\nu_i \times x_i}{\sum_i \nu_i \times x_i} \quad (2)$$

$$r_i = \nu_i \frac{x_i \times F_{total}}{m_{cat} \times 22.4} \quad (3)$$

In the test involving a mixed $CO/CO_2/H_2/N_2$ feed, the following equations were employed for the CO_x conversion and product selectivity calculations:

$$X(CO_x) = \frac{x_{CH3OH}^{out} + x_{CO}^{out} - x_{CO}^{in}}{x_{CO}^{in} + x_{CO_2}^{in}} \quad (4)$$

$$S(CO) = \frac{x_{CO}^{out} - x_{CO}^{in}}{x_{CO}^{out} - x_{CO}^{in} + x_{CH3OH}^{out}} \quad (5)$$

$$S(CH_3OH) = \frac{x_{CH3OH}^{out}}{x_{CO}^{out} - x_{CO}^{in} + x_{CH3OH}^{out}} \quad (6)$$

In eqs 1-6, ν_i is the number of C atoms in product i. x_i is the molar fraction of product i in the outlet, x_i^{in} and x_i^{out} are the molar fraction of product i in the inlet and outlet, and x_{CO}^{in} and $x_{CO_2}^{in}$ are the molar fraction of CO and CO_2 in the inlet, respectively. m_{cat} is the catalyst mass and F_{total} is the feed gas volumetric flow rate.

3. RESULTS AND DISCUSSION

3.1. Catalyst Characterization. The content of Pd and Cu experimentally determined by the ICP OES method is about 1.0 and 5.0 wt % (Table S1), respectively, and is close to the nominal values. However, the content of Zn is slightly lower, i.e., 2.3 wt % versus 2.5 wt %. The specific surface area (S_{BET}) of the catalysts containing solely Pd does not appear to be significantly influenced by the kind of support (CeO_2, $Ce_{0.8}Zr_{0.2}O_2$, or CeO_2−SiO_2) and is between 56 and 64 m^2·g^{-1} (Table S1). The addition of Cu and Zn resulted in a slight decrease in S_{BET} to around 48 m^2·g^{-1}. The catalysts containing Pd or CuZnPd on ZrO_2 exhibited a slightly higher S_{BET}, i.e., 76−77 m^2·g^{-1}.

No crystalline Pd-containing phase was detected in the samples having either supported Pd or CuZnPd species (Figure S2). The main phase detected in the Ce-containing materials with Pd was cubic CeO_2. It should be noted that the main reflections of this phase coincide with those of $Ce_{0.8}Zr_{0.2}O_2$, making it impossible to distinguish between the phases (Figure S2a). The monoclinic CuO and hexagonal ZnO phases were identified in the CuZnPd-CeZr, CuZnPd-CeSi catalysts (Figure S2c). The monoclinic and tetragonal ZrO_2 phases were determined in the Pd−Zr catalyst (Figure S2b). The CuZnPd-Zr catalyst contains the monoclinic ZrO_2 phase (Figure S2d). Although the hexagonal ZnO phase was detected in this sample, no crystalline Cu phases were observed, in contrast to other CuZnPd-based catalysts.

3.2. Redox and Basic Properties of the Catalysts. To investigate the redox properties of the materials developed, H_2-TPR tests were performed (Figure 1a). The H_2 consumption profiles of bare supports exhibited distinct differences (Figure S3a). ZrO_2 was not reduced over the entire temperature range,

https://doi.org/10.1021/acscatal.4c07462
ACS Catal. 2025, 15, 2328−2341

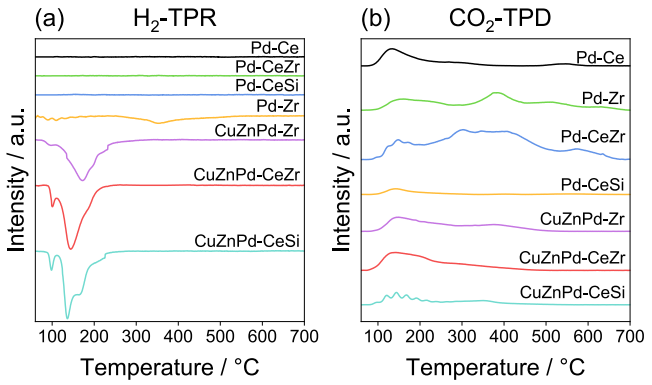

Figure 1. (a) H_2-TPR and (b) CO_2-TPD profiles of fresh supported Pd- and CuZnPd-based catalysts. The measurements were conducted within a temperature range of 50 and 700 °C.

whereas supports containing cerium consumed H_2, which is characteristic of CeO_2 reduction.[36] The total consumption of H_2 determined for the latter material was approximately 0.5 mmol·g^{-1} (Figure S3b). Surprisingly, the Ce-based catalysts containing Pd showed negligible H_2 consumption. It is likely that the sample reduction occurred at a lower temperature, as was found for Pd/CeO_2(cubic) by Tan et al.[46] The consumption peak in their work was found at 31 °C, below the beginning of our measurements, which commenced at 50 °C. Conversely, the Pd−Zr catalyst consumed H_2 in the temperature range of 300−400 °C resulting in an overall H_2 consumption of about 0.4 mmol·g^{-1} (Figure S4a). The consumption is likely related to the removal of lattice oxygen from ZrO_2.[47] Supported Pd species are supposed to be involved in the activation of gas-phase H_2 yielding surface atomic species, which spill over to the surface of the support and react with lattice oxygen. Significantly higher H_2 consumption was observed across all catalysts containing Cu, Zn, and Pd. The maximum H_2 consumption was achieved between 100 and 200 °C, being lower than for the reduction of CuO in CuZn-based catalysts, which typically require 200 to 300 °C.[20] This observation suggests that the combination of Pd and Cu leads to a significant improvement in the CuO reducibility, probably due to the well-known ability of Pd to activate gas-phase H_2.[48]

All catalysts possess basic sites as concluded from the CO_2-TPD profiles (Figure 1b). The presence of ZrO_2 in the support appears to be favorable for CO_2 adsorption. The highest amount of desorbed CO_2 of about 4.4 μmol·m^{-2} was determined for the Pd-CeZr catalyst (Figure S4b). ZrO_2 also increases the strength of basic sites. In contrast, the presence of SiO_2 in the support is detrimental for catalyst basicity.

3.3. Catalytic Performance at Different Reaction Temperatures. To assess the performance of either Pd or CuZnPd-containing catalysts in CO_2 hydrogenation to methanol, tests were conducted at temperatures of 160−225 °C, a pressure of 20 bar, and a $\tau_{modified}$ of 900 mL·g_{cat}^{-1}·h^{-1} using a $CO_2/H_2/N_2$ = 3/9/1 feed (Figure 2). Irrespective of the support type, the former catalysts showed higher CO_2 conversion with the exception at 225 °C, where the conversion over Pd−Zr and CuZnPd-Zr was very similar. Among the catalysts containing only Pd, Pd−Ce was the least active catalyst (Figure S5a). If the support material contained

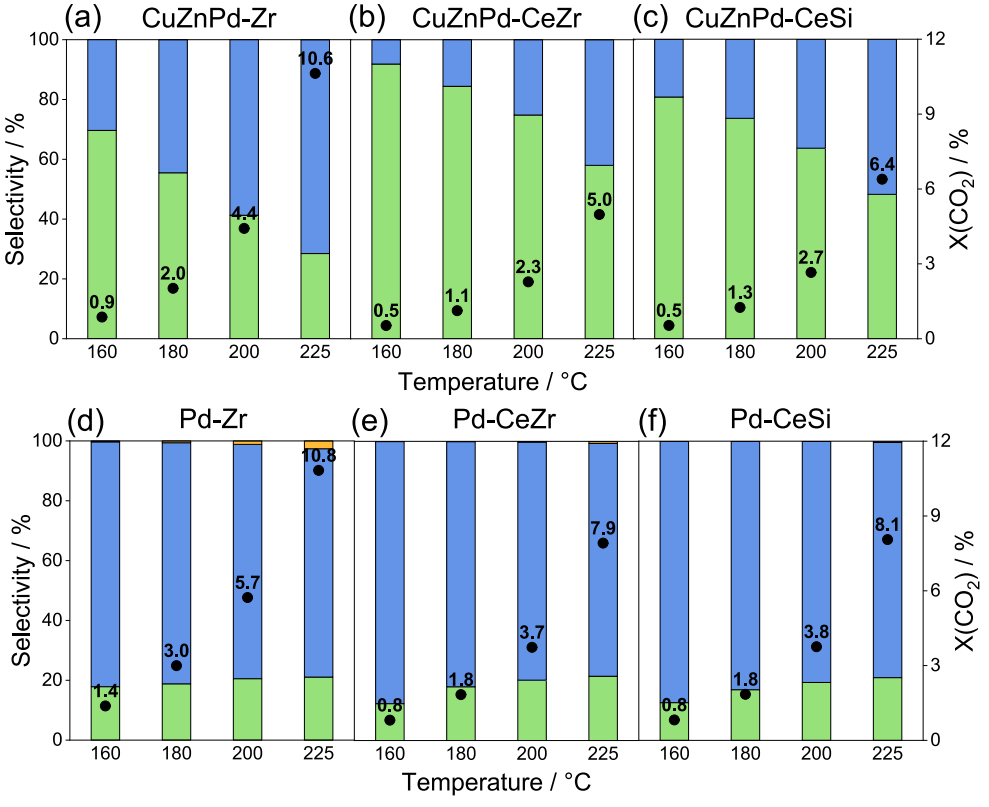

Figure 2. Product selectivity (bars, left axis) and CO_2 conversion (dots, right axis) obtained over the (a-c) CuZnPd/support and (d-f) Pd/support catalysts at different temperatures. Green − CH_3OH, blue − CO, and orange − CH_4. Reaction conditions: 20 bar, 250 mg, 4 mL·min^{-1}, $CO_2/H_2/N_2$ = 3/9/1, $\tau_{modified}$ ∼ 900 mL·g_{cat}^{-1}·h^{-1}.

https://doi.org/10.1021/acscatal.4c07462
ACS Catal. 2025, 15, 2328−2341

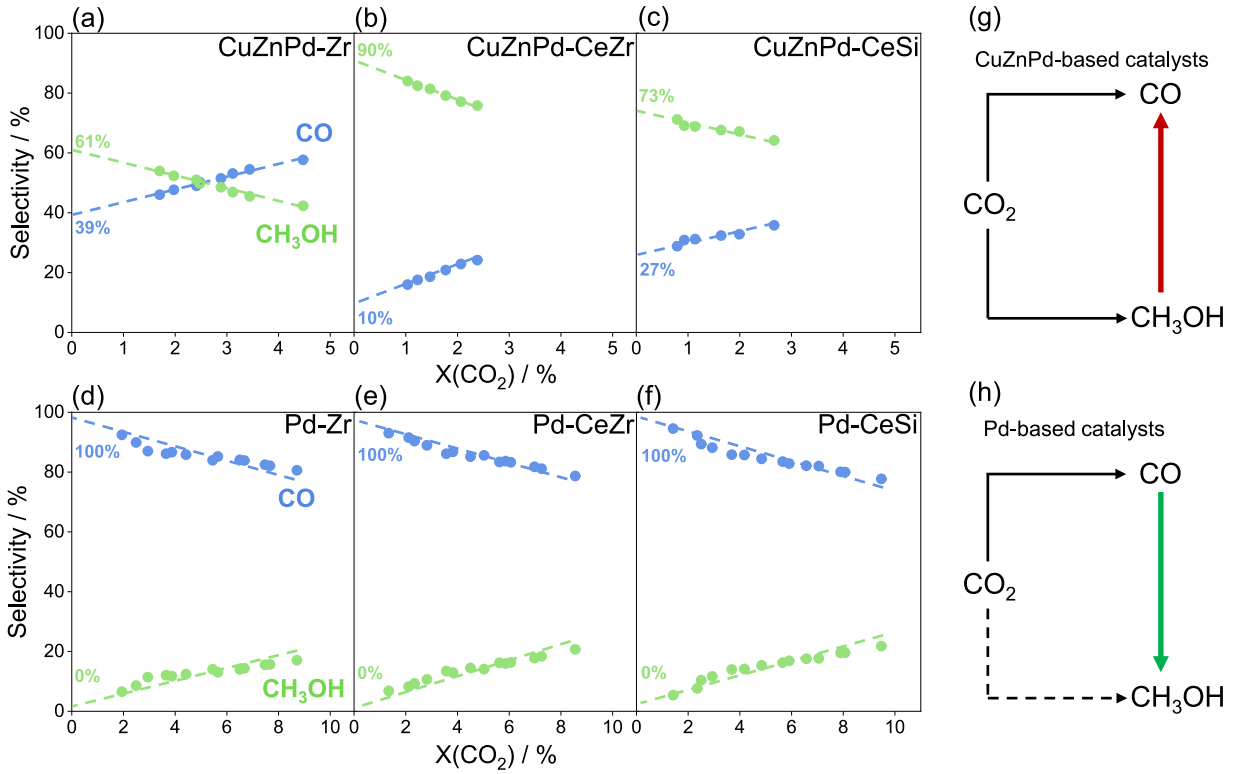

Figure 3. Dependence of CO and CH_3OH selectivity on the CO_2 conversion over (a-c) CuZnPd/support and (d-f) Pd/support catalysts. Green symbols − CH_3OH and blue symbols − CO. Reaction pathways over (g) CuZnPd/support and (h) Pd/support catalysts. The dashed line in (h) represents a minor possible pathway. Reaction conditions: 20 bar, 200 °C, (a-c) 150−250 mg, 4−11 mL·min^{-1}, $\tau_{modified}$ 900−4600 mL·g_{cat}^{-1}·h^{-1}, $CO_2/H_2/N_2$ = 3/9/1, (d-f) 100−500 mg, 6−21 mL·min^{-1}, $\tau_{modified}$ 700−12400 mL·g_{cat}^{-1}·h^{-1}, $CO_2/H_2/N_2$ = 1/3/4.

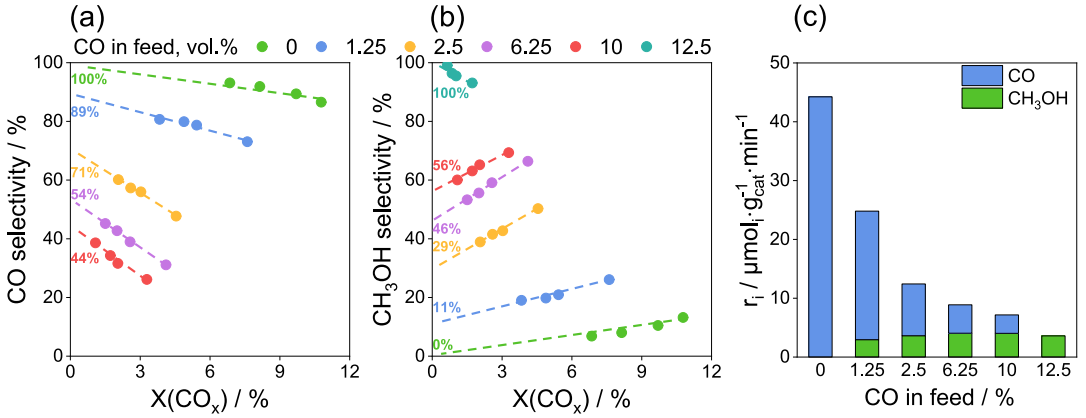

Figure 4. Selectivity-CO_x-conversion relationships for (a) CO and (b) CH_3OH; and (c) CO and CH_3OH formation rates over the Pd−Zr catalyst. Reaction conditions: 200 °C, 50 bar, 3 g, 90−300 mL·min^{-1}, $CO/CO_2/H_2/N_2$ = x/12.5-x/37.5/50 vol %, there CO and CO_2 fractions changing from 0 to 12.5 vol % for CO and reverse for CO_2. (a, b) The numbers at zero CO_x conversion stand for the primary selectivity to CO or CH_3OH. (c) Detailed calculations are provided in the Supplementary Note.

additionally zirconia or silica, the conversion of CO_2 was about 1.6 times higher. Furthermore, the catalysts containing only Pd were prone to form predominantly CO, while the main product over the catalysts with CuZnPd was methanol. In addition, Pd−Zr (Figure 2d) or Pd−Ce (Figure S5a) produced methane above 200 °C or in the entire temperature range of 160−225 °C, respectively. This undesired reaction was strongly hindered when the support consisted of CeZr or CeSi (Figure 2e,f).

While no significant support effect on product selectivity was noted for Pd-containing catalysts (Figures 2d-f and S5a), the presence of Ce in the support seems to be important for the selectivity to CH_3OH over CuZnPd-containing catalysts (Figure 2a-c). This experimental observation agrees with a previous study, which was aimed to identify important descriptors affecting CH_3OH selectivity through analyzing available literature data.[16]

3.4. Reaction Pathways of Product Formation. To understand the fundamentals of distinctive product selectivity obtained over the Pd- or CuZnPd-containing catalysts, additional CO_2 hydrogenation tests were performed at 200 °C and 20 bar but different $\tau_{modified}$ (700−12400 mL·g_{cat}^{-1}·h^{-1}). Both the catalyst amount and the feed total flow rate were changed, while the feed composition was constant. The

https://doi.org/10.1021/acscatal.4c07462
ACS Catal. 2025, 15, 2328−2341

obtained selectivity and CO_2 conversion values were used to construct selectivity-conversion relationships for CO and CH_3OH (Figures 3 and S5b). As CH_4 was formed in negligible amounts, the corresponding selectivity-conversion profile was not analyzed.

The key dissimilarity between the two catalyst groups lies in the origins of CO or CH_3OH. These products are formed in parallel from CO_2 over the CuZnPd-based catalysts as can be concluded from nonzero selectivity values for these products at zero CO_2 conversion (Figure 3a-c). In addition to these two parallel pathways, CH_3OH undergoes consecutive transformation(s) to CO. This conclusion is based on the fact that the selectivity to CO increases, while the selectivity to CH_3OH decreases with increasing CO_2 conversion. Such selectivity-conversion relationship is typical for various CuZn-based catalysts.[18,22] On the contrary, the catalysts containing Pd as the only active component do not seem to produce CH_3OH from CO_2 as indicated by about 100% CO selectivity at near to zero CO_2 conversion (Figures 3d-f and S5b). As the CO selectivity decreases with rising CO_2 conversion while the selectivity to CH_3OH increases, the desired alcohol must be formed through CO hydrogenation. This observation suggests the potential for controlling the methanol formation pathway to circumvent decomposition issues over Cu-containing catalysts. In summary, two different reaction schemes are valid for product formation in the course of CO_2 hydrogenation over CuZnPd-based and Pd-based catalysts (Figure 3g,h).

3.5. Performance of Pd−Zr with Cofed CO. To validate the hypothesis about the formation of CH_3OH from CO over the Pd−Zr catalyst, additional tests using feeds composed of different amounts of CO_2 and CO were performed. It is important to note that the total fraction of these reactants remained at 12.5 vol % to maintain the H_2/CO_x ratio at 3. Figure 4 depicts the selectivity-conversion relationships obtained at 200 °C and 50 bar. The primary (extrapolated to zero CO_x conversion) selectivity to methanol was 100% when the feed contained CO only. It decreased with rising CO conversion due to the hydrogenation of CH_3OH to CH_4 (Figure S6). The formation of trace amounts of dimethyl ether and methyl formate was also observed, yet the corresponding selectivity-conversion profiles were not subjected to analysis. No CO_2 was formed. It should be especially mentioned that the outlet concentration of CO in tests using feeds consisting of CO and CO_2 was higher than the inlet concentration. In other words, although CO from the feed was hydrogenated to CH_3OH, CO_2 produced a higher amount of CO through RWGS. Consequently, the primary selectivity to CH_3OH decreased when the fraction of CO in CO_x was lowered from 100% to 10%. Nevertheless, for all feeds containing CO and CO_2, the selectivity to methanol increased as the conversion of CO_x increased. The observed increase can be attributed to the kinetics of CO and CH_3OH formation through the RWGS reaction and CO hydrogenation, respectively, as indicated by the dependence of the ratios of the outlet fractions of these products on $\tau_{modified}$ (Figure S7). Although they both increase with decreasing $\tau_{modified}$, the strength of the increase is more pronounced for CH_3OH. This is due to the different thermodynamic constraints for the RWGS reaction and CO hydrogenation (Figure S8).

We also determined the initial rates of CO and CH_3OH formation in the above tests (Figures 4b,c and S1, and Supplementary Note). When only CO_2 was present in the feed as the carbon source, CO was the sole product with a formation rate of about 44 $\mu mol \cdot g_{cat}^{-1} \cdot h^{-1}$, while the methanol formation rate from CO_2 was zero (Figure 4c). Methanol was clearly observed as one of the primary products (Figure 4b) with a formation rate of about 2.9 $\mu mol \cdot g_{cat}^{-1} \cdot h^{-1}$ when a small part of CO_2 in the reaction feed was replaced by CO, i.e., 1.25 vol % CO and 11.25 vol % CO_2 in the feed (Figure 4c). As the CO fraction in the feed further increased, the rate of CO formation from CO_2 significantly decreased, while the rate of CH_3OH formation increased from 2.9 to 4.1 $\mu mol \cdot g_{cat}^{-1} \cdot h^{-1}$ using a feed with the ratio of CO/CO_2 of 1. Further increasing the concentration of CO in the feed at the expense of CO_2 resulted in a slight decrease in the rate of methanol formation. The negative effect of cofed CO on the rate of CO formation is explained by hindering the RWGS reaction.

3.6. Redox and Structural Catalyst Properties. In order to check whether the different performance of CuZnPd- and Pd-based materials is influenced by catalyst basic properties or reducibility, a correlation was sought between the rates of CO and CH_3OH formation and the amounts of CO_2 desorbed in CO_2-TPD tests or H_2 consumed in H_2-TPR tests (Figure S9a,b). However, no obvious correlation could be obtained. Additionally, the specific surface area of the catalysts was not found to have a noticeable impact on the activity (Figure S9c).

Scanning transmission electron microscopy (STEM) coupled with energy-dispersive X-ray spectroscopy (EDX) was also used to analyze the Pd−Zr and CuZnPd-Zr catalysts. Given the negligible effect of the support on the performance of sole Pd-containing catalysts, these catalysts were selected to minimize the complexities arising from the diverse composition of different supports. As anticipated, the ZrO_2 support exhibits a high degree of similarity in both samples (Figure S10). Given the similar or lower atomic weight of Pd, Zn, and Cu, relative to Zr, the former elements are not discernible by contrast in the high-angle annular dark field (HAADF) or annular bright field (ABF) images. Consequently, conclusions can only be drawn from EDX mapping measurements. It appears that Pd is distributed relatively evenly over the support in Pd−Zr (Figures S11 and S12), it is, however, not possible to determine whether Pd is present as highly dispersed species or as clusters. The CuZnPd-Zr catalyst appears to be more complex. While Zn is predominantly highly dispersed over the support, Cu is present in the form of highly dispersed species and larger agglomerates (Figure 5). It is noteworthy that Pd was observed in small quantities in the regions exhibiting agglomerated/enriched Cu, indicating a potential spatial proximity of Cu and Pd (Figures 5 and S13). Moreover, the EDX peaks for Cu and Zn appear to correlate in regions with distributed Cu, suggesting a possible spatial proximity of these two elements in the remaining regions of the material (Figure S13c).

3.7. Local Structure and Electronic Properties. The surface composition and valence state of Cu, Zn, Pd, and Zr were assessed by pseudo in situ XPS tests. The Pd signal in the XP spectra of the CuZnPd-Zr and Pd−Zr catalysts was barely discernible due to the low Pd loading (1 wt %Pd) and the overlap with two intense Zr 3p peaks in the same binding energy region (Figure S14a,e). The Pd $3d_{5/2}$ and Pd $3d_{3/2}$ signals at 335.5−335.7 eV and 340.7−341.0 eV, respectively, correspond to metallic Pd^0 and are present in the XP spectra of reduced and spent catalysts.[49−51] In the Zr 3d region (Figure S14b,f), the Zr $3d_{5/2}$ and Zr $3d_{3/2}$ peaks at 182.3 eV and 184.6−184.7 eV are characteristic of Zr^{4+} in ZrO_2.[52] The

https://doi.org/10.1021/acscatal.4c07462
ACS Catal. 2025, 15, 2328−2341

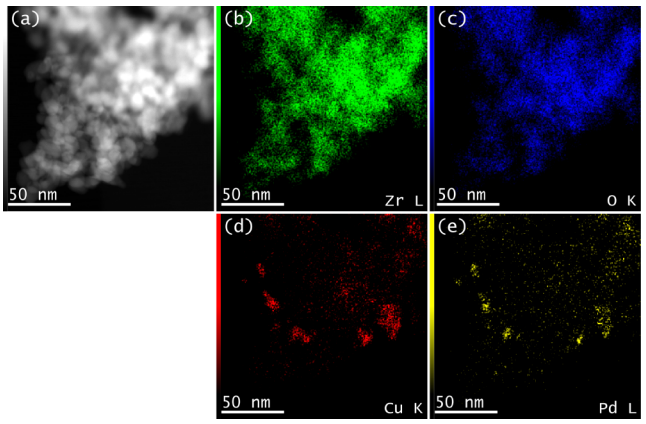

Figure 5. EDX elemental mapping of CuZnPd-Zr. Cu is visible in both distributed and agglomerated forms. While Pd is predominantly present at the same positions as agglomerated/enriched Cu, Zn appears to be present only in distributed form (see also Figure S13). Due to low intensity of the Zn K_α signal at each pixel, this map is not displayed.

minor shifts (~+0.1 eV) in these binding energy values between the freshly reduced and spent samples are well within the typical binding energy error of ±0.3 eV but could also be caused by a weak metal−support interactions (MSI) during the catalytic process.[25] In general, ZrO_2 acts as a stable support in both catalysts, with minimal structural degradation. In comparison with the XP spectra of fresh Pd−Zr and CuZnPd-Zr catalysts in the O 1s region (Figure S14c,g), the signals characteristic of lattice oxygen, at 529.6 and 530.1 eV, and the surface oxygen/hydroxyl species, at 531.4 and 531.7 eV, respectively, exhibited slight shifts to higher binding energies in the spent samples. In addition, the intensity of the signal related to surface oxygen/hydroxyl species increased. Such changes may be attributed to a higher number of oxygen vacancies and adsorbed intermediates formed during the reaction.[53−55] The distinction between the Pd−Zr and CuZnPd-Zr catalysts is minimal, with the exception of a slightly elevated intensity of surface oxygen/hydroxyl species peak in the XP spectrum of spent CuZnPd-Zr. This suggests that the addition of Cu-ZnO improves the formation of oxygen vacancies and surface intermediates. Regardless of the kind of catalyst state (reduced or spent), Cu^{1+}/Cu^0 (932.6 and 952.4 eV) are the main states of copper (Figure S14d). The absence of the characteristic satellite peaks around 940−944 eV provides compelling evidence that all Cu^{2+} species have been reduced.[25,56] In contrast, Zn^{2+} has not changed its oxidation state after catalyst reduction and throughout the course of the

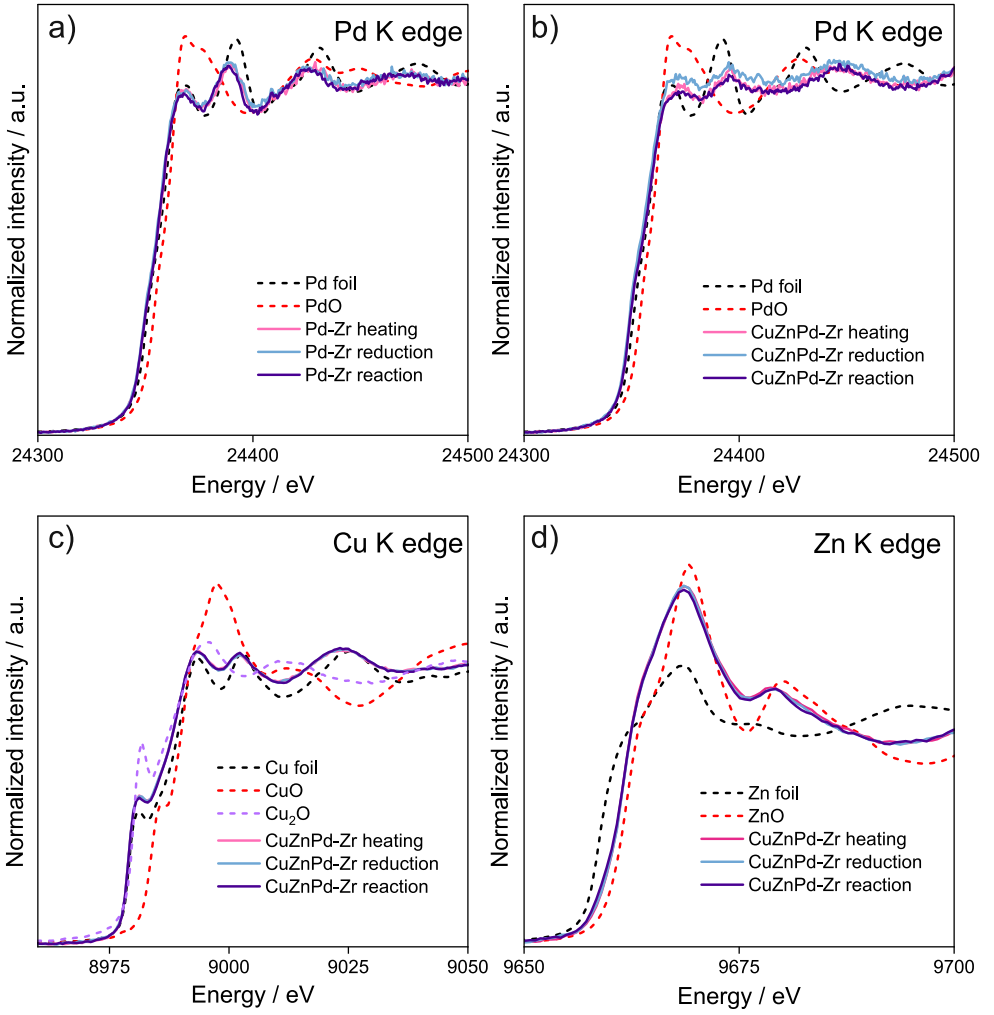

Figure 6. Pd K edge XANES spectra of (a) Pd−Zr and (b) CuZnPd-Zr, (c) Cu K edge XANES of CuZnPd-Zr, and (d) Zn K edge XANES of CuZnPd-Zr obtained in He during heating, in 50 vol % H_2 in He during reduction (at 300 °C), and in CO/H_2 during reaction (at 200 °C).

https://doi.org/10.1021/acscatal.4c07462
ACS Catal. 2025, 15, 2328−2341

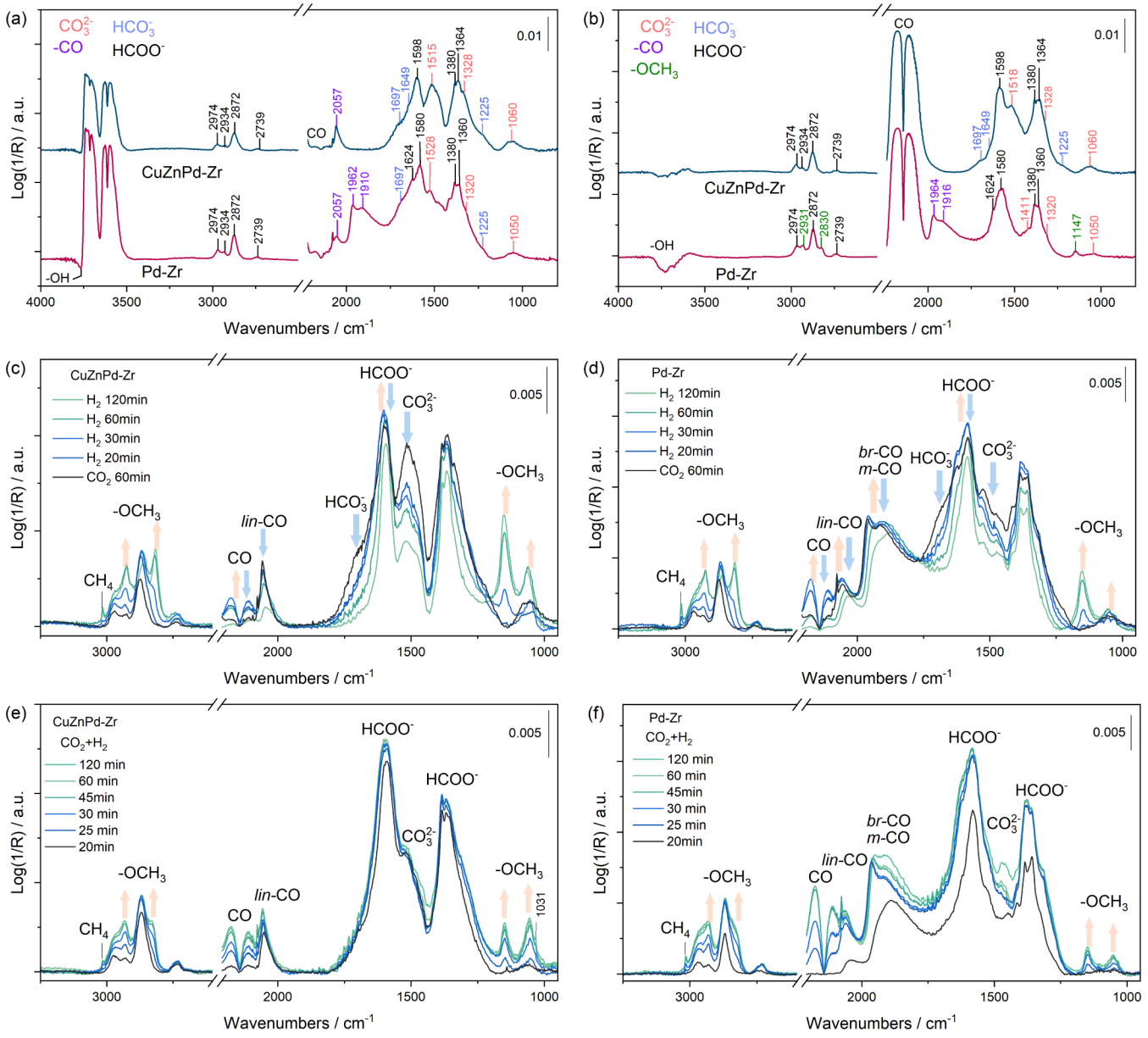

Figure 7. DRIFT spectra of the CuZnPd-Zr and Pd−Zr catalysts recorded after 60 min exposure to (a) CO_2 (22 vol % in He), (b) CO (5 vol % in He), (c, d) H_2 (50 vol % in He) after CO_2 treatment, and (e, f) the 22 vol %CO_2/66 vol %H_2/He reaction mixture at 200 °C and 20 bar. The orange arrows indicate increasing band intensity, blue down arrows indicate decreasing band intensity.

reaction as concluded from the presence of Zn^{2+} peaks (1022.1 and 1045.2 eV) in the Zn 2p region (Figure S14h).[56,57]

The XANES spectra provide insights into the oxidation and alloying states of Pd, Cu, or Zn in Pd−Zr and CuZnPd-Zr catalysts under various treatment conditions (Figure 6). In the fresh Pd−Zr catalyst (Figure 6a), the initial oxidation state of Pd is observed to be between 0 and +2. Upon subsequent heating in He, exposure to H_2 and CO/H_2, the Pd state becomes largely metallic, exhibiting only a slight shift relative to the Pd foil reference. The Fourier transformed EXAFS spectra and EXAFS fitting results are presented in Figures S15−17 and Table S2. The increased Pd−Pd distance in the Pd−Zr sample in the presence of H_2 may be indicative of the formation of a small fraction of PdH_x (Table S2). In contrast, the Pd edge in CuZnPd-Zr (Figure 6b) exhibits a distinctive behavior. Following calcination, the oxidation state of Pd is observed to be +2. However, upon heating in He, reduction, and during the CO/H_2 reaction, the oscillations at 24392 and 24430 eV broaden and shift to higher energies. Such changes suggest formation of an alloy or intermetallic PdCu and/or PdZn phase(s). The in situ Pd K edge FT EXAFS spectra of the CuZnPd-Zr catalyst (Figure S15b) demonstrates a single, relatively narrow peak at approximately 2.2 Å (uncorrected distance), which is significantly different from the Pd foil, the Pd−Zr data, and the spectra of PdZn intermetallics previously reported,[41] and corresponds to backscattering on a 3d metal atoms only. The backscatter may, in theory, be attributed to both Cu and Zn, given that their atomic form factors are very similar. However, all known PdZn alloys or intermetallic compounds would also exhibit Pd−Pd scattering paths in the first coordination shell, which is not visible in the current case. For the Cu K edge in CuZnPd-Zr (Figure 6c), the initial oxidation state of Cu is likely to be +2. Upon heating in He, the CuO_x species are reduced to metallic Cu, as evidenced by

https://doi.org/10.1021/acscatal.4c07462
ACS Catal. 2025, 15, 2328−2341

the same edge position and the same set of features as in Cu foil reference spectrum. Additionally, the peak positions in the Cu K XANES spectrum shift to lower energies, potentially indicating the formation of a PdCu alloy. The fits of Pd K and Cu K edges EXAFS spectra confirm the incorporation of Pd in the fcc Cu lattice, which is likely to be a random PdCu alloy (Figures S15−17 and Tables S3 and S4). No significant alterations in the spectral profiles are observed during exposure to H_2 and syngas, suggesting that the metallic state remains stable under these conditions. At the Zn edge (Figure 6d), the initial oxidation state of Zn is observed to be +2. The Zn spectrum exhibits minimal changes across different treatments, including heating, reduction, and reaction, with a slight decrease in the intensity of the white line compared to the fresh catalyst. This suggests a minor reduction of ZnO, which may contribute to the formation of PdZn. The characteristic feature at 9669 eV appears considerably broader than that of pure ZnO, suggesting a lower degree of ordering of ZnO_x species in the catalyst compared to bulk ZnO, which may be attributed to a phase transformation to graphitic ZnO.[58]

3.8. In Situ DRIFTS Study of Pd−Zr and CuZnPd-Zr Catalysts. Using in situ DRIFTS, various types of carbonates, bicarbonates, carbonyls, and formates were identified on the surface of the Pd−Zr and CuZnPd-Zr catalysts upon their exposure to CO_2 at 200 °C and 20 bar for 1 h (Figure 7a,b and Table S5). The bands in the ranges of 1550−1410, 1328−1320, 1060−1055 cm^{-1} correspond to bidentate, *bi*-CO_3^{2-}, monodentate, *m*-CO_3^{2-}, and polydentate, *p*-CO_3^{2-}, carbonates, respectively.[59−62] The bands at 1550−1430 cm^{-1} are more intense in the spectrum of the CuZnPd-Zr catalyst compared to the Pd−Zr catalyst probably due to the presence of additional carbonate/carboxylate species stabilized on Cu-ZnO oxide species/phases. The bands, characteristic of bidentate formate species, *bi*-$HCOO^-$, are also observed in the spectra of the CuZnPd-Zr and Pd−Zr catalysts at 1598/1364 and 1580/1360 cm^{-1}, respectively.[63−67] In addition, bicarbonates, HCO_3^-, with bidentate and monodentate configurations are present on the surface of these catalysts, as evidenced by the presence of bands at 1697/1649/1225 cm^{-1}. Their formation can occur through the interaction of CO_2 with OH hydroxy species as previously reported for ZrO_2.[60] In agreement, we observed a negative band at ∼3770 cm^{-1} for both catalysts.

CO_2 was also observed to dissociate to CO, which is present in the form of gaseous CO and surface carbonyls (Figure S18a,b).[68] Three kinds of the carbonyls, linear, bridged, and multidentate configurations (*lin*-CO/*br*-CO/*m*-CO), with the characteristic bands at 2057/1962/1910 cm^{-1} should be present on the surface of the Pd−Zr catalyst.[69−71] In the case of the CuZnPd-Zr catalyst, only *lin*-CO species (band at 2057 cm^{-1}) were formed. The difference between the catalysts should be related to the distribution of Pd species. *lin*-CO species are suggested to be stabilized on very small Pd[69,72] or bimetallic Pd-containing particles.[73−75] The latter are present on the surface of the CuZnPd-Zr catalyst (Figure 5).

The intermediates that can originate from CO were also studied (Figure 7b). Due to the interaction of CO with surface oxygen/hydroxy groups, CO_3^{2-} and HCO_3^- can be formed,[76,77] which were detected on the surface of the CuZnPd-Zr catalyst only. Furthermore, the introduced CO was also oxidized to gaseous CO_2 by lattice oxygen of ZrO_2 and/or $CuZnO_x$, with this reaction being more pronounced for the Pd−Zr catalyst (Figure S18c,d). Moreover, OCH_3 was formed over this catalyst as evidenced by the appearance of bands at 2931/2830/1147 cm^{-1}, whereas no corresponding signals are present in the spectrum of the CuZnPd-Zr catalyst.

Further possible transformations of the adsorbed species formed from CO_2 upon their reaction with H_2 were also analyzed (Figure 7c,d). For both samples, a decrease in the number of CO_3^{2-} and HCO_3^- species was observed, while the concentration of gaseous CO and $HCOO^-$ initially increased (Figure S19a,b). It was previously proposed that HCO_3^- could transform into CO, and that CO_3^{2-} could be directly hydrogenated to $HCOO^-$.[78] In our experiments, as CO_3^{2-} and carbonyl species remained on the surface after the disappearance of HCO_3^- and gaseous CO, the latter product should be formed from HCO_3^-. The carbonyl band intensities for the Pd−Zr sample initially increased as a result of an increased amount of gaseous CO, and subsequently decreased (Figures 7c,d and S19a,b). In contrast, the intensity of *lin*-CO band in the spectrum of the CuZnPd-Zr sample consistently decreased with rising time on H_2 stream, indicating a higher rate of H_2-induced transformation of *lin*-CO than that of CO adsorption to yield *lin*-CO. For both catalysts, OCH_3 species and CH_4 were observed. The intensity of the CH_4 bands relative to the OCH_3 bands was higher for Pd−Zr than for CuZnPd-Zr (Figure S19c,d). This is also in a good agreement with the results of the catalytic tests (Figure 2a,d).

In situ DRIFTS measurements, conducted with a CO_2/H_2/He feed (22/66/12 vol %) at 200 °C and 20 bar, revealed the presence of the same set of adsorbates as observed after CO_2 adsorption (Figure 7e,f). However, the quantity of surface HCO_3^- and CO_3^{2-} species under reaction conditions appears to be lower in comparison with CO_2 adsorption experiments in the absence of H_2 due to the rapid transformation of these species to CO and $HCOO^-$ in the presence of H_2. For CuZnPd-Zr, a steady-state concentration of $HCOO^-/CO_3^{2-}$/*lin*-CO species was achieved after 20 min exposure to the reaction feed. Concurrently, the concentration of OCH_3 species and gaseous CO, CH_4, and CH_3OH (at 1031 cm^{-1})[63,79] increased throughout the whole experiment (Figures 7e and S20). In contrast to the CuZnPd-Zr catalyst, no steady-state concentration of $HCOO^-$ was achieved and a higher number of surface carbonyls on the metallic Pd particles was detected in the tests with the Pd−Zr catalyst during its treatment in the reaction feed (Figure S20b). The analysis of the intensity of the bands characteristic of surface OCH_3 and gaseous CO and CH_4 (Figure S20d) revealed a significantly higher amount of formed gaseous CO relative to OCH_3 and CH_4 under the reaction conditions for the Pd−Zr sample, indicating its higher activity in CO formation.

3.9. Mechanistic Aspects of Product Formation over Pd- and CuZnPd-Containing Catalysts. The results (Figures 3d−f and S5b) presented in section "**Catalytic performance**" and their discussion corroborate the overall reaction scheme of product formation in CO_2 hydrogenation, illustrated in Figure 3h. CO_2 does not appear to be the gas-phase precursor of methanol over Pd/support catalysts. Instead, it is converted almost exclusively to gas-phase CO through the RWGS reaction. Subsequently, this product is then involved in secondary transformations, leading to the desired alcohol. The participation of adsorbed CO formed from CO_2 in the formation of methanol can be excluded because the selectivity to methanol extrapolated to zero CO_2 conversion in tests with a CO_2/H_2 feed would not be zero as we determined experimentally (Figures 3d-f, 4b). Based on these findings, it can be inferred that the sites responsible for the formation of

https://doi.org/10.1021/acscatal.4c07462
ACS Catal. 2025, 15, 2328−2341

CO from CO_2 and for the conversion of CO to methanol must be distinct. In contrast to the Pd/support catalysts, the CO_2 conversion over the CuZnPd-based catalysts primarily involves the hydrogenation of CO_2 to CH_3OH and CO. If the latter product would be further hydrogenated to CH_3OH with a significant rate, the selectivity to this alcohol would increase with rising CO_2 conversion, In contrast, this selectivity decreases as the primarily formed CH_3OH undergoes decomposition to CO (Figure 3a,b,c,g) in agreement with previous studies using different CuZn-containing catalysts.[17,18]

Based on the above discussion and the results of the in situ FTIR tests, we suggest reaction schemes to explain the discrepancy between the Pd- and CuZnPd-containing catalysts in the pathways of CO and CH_3OH formation. CO_2 adsorbs on the CuZnPd-Zr surface preferentially in the form of $HCOO^-$ species (Figure 7). In accordance with previous studies,[4,20] methanol is formed through the following sequence of transformations $HCOO^-(s) \rightarrow OCH_3(s) \rightarrow CH_3OH$ (g) (Scheme 1). In addition, we propose that *lin*-CO species are precursors of gaseous CO.

Scheme 1. Proposed Pathways for CO_2 Hydrogenation to Methanol over the Pd−Zr (Top) and CuZnPd-Zr (Bottom) Catalysts Based on the Observations from STEM/EDX, XANES, EXAFS, and DRIFTS Measurements

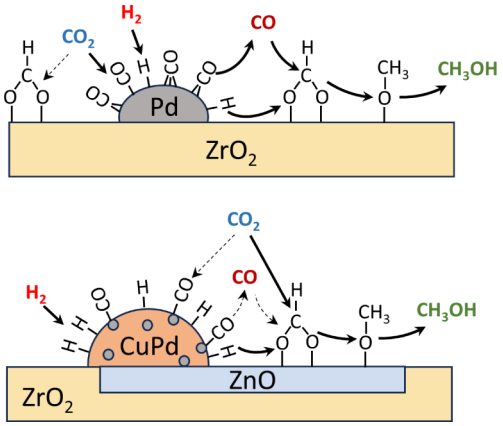

In contrast to the CuZnPd-Zr catalyst, the Pd−Zr catalyst can form OCH_3 from CO (Figure 7b). As the bands related to the former species on the surface of these two catalysts are characterized by different wavenumbers (Figure 7c,d and Table S5), it can be suggested that OCH_3 is stabilized on ZrO_2 and Cu-ZnO in the case of the Pd−Zr and CuZnPd-Zr catalysts, respectively. Based on these observations, we suggest a two-step mechanism of CH_3OH formation in CO_2 hydrogenation over the Pd−Zr catalyst (Scheme 1). Gas-phase CO_2 initially dissociates on the surface of the catalysts as follows $CO_2(g) \rightarrow CO(s)+O(s)$. This process is expected to occur on Pd species. As gaseous CO is the primary source of CH_3OH over this catalyst (Figure 3), CO adsorbed on Pd should desorb. However, if the formed gas-phase CO readsorbed on the same sites, where CO_2 decomposition occurred and subsequently participated in the methanol formation, the latter selectivity extrapolated to zero CO_2 conversion would not be zero, which is contrary to the experimental results. Thus, the sites of methanol formation should differ from those yielding CO from CO_2. We suggest that the methanol formation should occur on the surface of the ZrO_2 support according to the following sequence $CO(g) \rightarrow HCOO^-(s) \rightarrow OCH_3{}^*(s) \rightarrow CH_3OH$ (g) (Scheme 1). The proposed scheme differs from the RWGS + CO-hydro mechanism of methanol formation,[80] because gas-phase CO but not adsorbed CO_2 or COOH species is involved in the formation of the aforementioned surface intermediates transforming to methanol. Furthermore, the ability of Pd to adsorb CO in various coordination modes (*lin*-CO/*br*-CO/*m*-CO) may also result in the occupation of the Pd centers, which would impede H_2 adsorption/dissociation and consequently decrease the rate of CO formation from CO_2 (Figure 4c).

4. CONCLUSIONS

The present study revealed the existence of distinct mechanisms of product formation in CO_2 hydrogenation to methanol over ZrO_2- or CeO_2-based catalysts with supported Pd or CuZnPd active components. The former species do not produce methanol from CO_2 but from gaseous CO. This product readsorbes on the surface of the support in the form of $HCOO^-$ species, which are further hydrogenated to methanol. Supported Pd species are responsible for the generation of adsorbed hydrogen species from H_2, which spill over to the support and are involved in the aforementioned hydrogenation. The addition of $CuZnO_x$ changes the reaction mechanism to a classical one, i.e., the formate route involving CO_2 directly, as $CuZnO_x$ demonstrate a greater propensity for the formation of formate species from CO_2 in comparison with Pd. Moreover, STEM/EDX, XANES, EXAFS, and in situ DRIFTS tests revealed that Pd species are in proximity of Cu or incorporated in the fcc Cu lattice, forming CuPd alloy. That is detrimental for the Pd to generate/stabilize carbonyls.

■ ASSOCIATED CONTENT

Supporting Information

The Supporting Information is available free of charge at https://pubs.acs.org/doi/10.1021/acscatal.4c07462.

Supplementary note with detailed calculations of product formation rates for $CO/CO_2/H_2/N_2$ test, CO_x conversion vs contact time for $CO/CO_2/H_2/N_2$ test over Pd−Zr, XRD patterns of samples, H_2-TPR results for fresh support materials, amounts of H_2 consumed and CO_2 desorbed during the H_2-TPR and CO_2-TPD, catalytic results for Pd−Ce, selectivity−conversion relationship over Pd−Zr in $CO/H_2/N_2$ feed, ratios of the outlet fraction over Pd−Zr, dependence of the equilibrium CO_x conversion on CO concentration in feed, correlations of H_2-TPR, CO_2-TPD, and BET results with product formation rates, selected HAADF-STEM images of Pd−Zr and CuZnPd-Zr, EDX elemental mapping of Pd−Zr, selected EDX spectrum of Pd−Zr, selected EDX spectrum of CuZnPd-Zr, XP spectra of Pd−Zr and CuZnPd-Zr, FT EXAFS spectra of Pd−Zr and CuZnPd-Zr at Pd K, Cu K, or Zn K edges, k^2-weighted EXAFS functions of Pd−Zr and CuZnPd-Zr at Pd K and Cu K edges, Fits of the FT EXAFS spectra of Pd−Zr and CuZnPd-Zr at Pd K and Cu K edges, DRIFT spectra measured during CO_2 and CO exposure over Pd−Zr and CuZnPd-Zr, band intensities of adsorbates in CO_2 exposure measurements over Pd−Zr and CuZnPd-Zr, band intensities of adsorbates in CO_2+H_2 exposure measurements over Pd−Zr and CuZnPd-Zr, table with BET and ICP OES characterization results, table with Pd K edge EXAFS fitting results of Pd−Zr, table with Pd K edge EXAFS fitting

https://doi.org/10.1021/acscatal.4c07462
ACS Catal. 2025, 15, 2328−2341

results of CuZnPd-Zr, table with Cu K edge EXAFS fitting results of CuZnPd-Zr, and table with observed band values from DRIFTS (PDF)

AUTHOR INFORMATION

Corresponding Authors

Sebastian Wohlrab − *Leibniz-Institut für Katalyse e.V., Rostock 18059, Germany*; orcid.org/0000-0003-1407-7263; Email: sebastian.wohlrab@catalysis.de

Evgenii V. Kondratenko − *Leibniz-Institut für Katalyse e.V., Rostock 18059, Germany*; orcid.org/0000-0003-0431-6937; Email: evgenii.kondratenko@catalysis.de

Authors

Denis Makhmutov − *Leibniz-Institut für Katalyse e.V., Rostock 18059, Germany*

Elizaveta Fedorova − *Leibniz-Institut für Katalyse e.V., Rostock 18059, Germany*

Anna Zanina − *Leibniz-Institut für Katalyse e.V., Rostock 18059, Germany*

Christoph Kubis − *Leibniz-Institut für Katalyse e.V., Rostock 18059, Germany*; orcid.org/0000-0001-9549-2455

Dan Zhao − *Karlsruher Institut für Technologie, Karlsruhe 76131, Germany*

Dmitry Doronkin − *Karlsruher Institut für Technologie, Karlsruhe 76131, Germany*; orcid.org/0000-0003-3930-3204

Nils Rockstroh − *Leibniz-Institut für Katalyse e.V., Rostock 18059, Germany*; orcid.org/0000-0001-6925-8577

Stephan Bartling − *Leibniz-Institut für Katalyse e.V., Rostock 18059, Germany*; orcid.org/0000-0001-5901-7235

Udo Armbruster − *Leibniz-Institut für Katalyse e.V., Rostock 18059, Germany*

Complete contact information is available at: https://pubs.acs.org/10.1021/acscatal.4c07462

Author Contributions

E.V.K. initiated and led the entire study. U.A., S.W., and E.V.K. acquired funding. D.M., A.Z., and E.V.K. wrote the first draft. E.F. and C.K. performed DRIFTS and analyzed the results. N.R. conducted and described the STEM/EDX measurements. S.B. performed XPS measurements. D.Z. and D.D. conducted XAS measurements and evaluated the results. All the authors discussed the results, improved the manuscript, and approved the final version of the manuscript.

Notes

The authors declare no competing financial interest.

ACKNOWLEDGMENTS

This work was supported by the Wissenschaftsgemeinschaft Gottfried-Wilhelm-Leibniz (WGL) in the frame of the SUPREME project (grant no. K308/2020). The authors would like to thank Daiichi Kigenso Kagaku Kogyu Co. Ltd., Japan, for providing the ZrO_2 material. The authors also thank Alexander Wotzka for the synthesis of the supports and Dr. Henrik Lund, Anja Simmula, and Reinhard Eckelt for XRD, ICP OES, and BET measurements, respectively. The authors would like to acknowledge DESY (Hamburg, Germany), a member of the Helmholtz Association HGF, for the provision of experimental facilities. Parts of this research were carried out at PETRA III, and the authors would like to thank Dr. Edmund Welter for assistance in using beamline P65. Beamtime was allocated for proposal I-20240122.

REFERENCES

(1) Morimoto, S.; Thuy, N.; Kitagawa, N.; Kataoka, S. Scenario assessment for producing methanol through carbon capture and utilization technologies considering regional characteristics. *J. CO2 Util.* **2021**, *45*, 101452.

(2) Atsbha, T. A.; Yoon, T.; Seongho, P.; Lee, C.-J. A review on the catalytic conversion of CO_2 using H_2 for synthesis of CO, methanol, and hydrocarbons. *J. CO2 Util.* **2021**, *44*, 101413.

(3) Battaglia, P.; Buffo, G.; Ferrero, D.; Santarelli, M.; Lanzini, A. Methanol synthesis through CO_2 capture and hydrogenation: Thermal integration, energy performance and techno-economic assessment. *J. CO2 Util.* **2021**, *44*, 101407.

(4) Zhong, J.; Yang, X.; Wu, Z.; Liang, B.; Huang, Y.; Zhang, T. State of the art and perspectives in heterogeneous catalysis of CO_2 hydrogenation to methanol. *Chem. Soc. Rev.* **2020**, *49* (5), 1385−1413.

(5) Zhou, W.; Cheng, K.; Kang, J.; Zhou, C.; Subramanian, V.; Zhang, Q.; Wang, Y. New horizon in C1 chemistry: breaking the selectivity limitation in transformation of syngas and hydrogenation of CO_2 into hydrocarbon chemicals and fuels. *Chem. Soc. Rev.* **2019**, *48* (12), 3193−3228.

(6) Makhmutov, D.; Zanina, A.; Kondratenko, E. V.; Wohlrab, S.; Armbruster, U. Effect of preparation conditions of molybdenum carbide catalysts on low-temperature CO_2 hydrogenation to methanol. *Catal. Today* **2024**, *441*, 114901.

(7) Guil-López, R.; Mota, N.; Llorente, J.; Millán, E.; Pawelec, B.; Fierro, J. L. G.; Navarro, R. M. Methanol Synthesis from CO_2: A Review of the Latest Developments in Heterogeneous Catalysis. *Materials* **2019**, *12* (23), 3902.

(8) Din, I. U.; Shaharun, M. S.; Alotaibi, M. A.; Alharthi, A. I.; Naeem, A. Recent developments on heterogeneous catalytic CO_2 reduction to methanol. *J. CO2 Util.* **2019**, *34*, 20−33.

(9) Dalena, F.; Senatore, A.; Marino, A.; Gordano, A.; Basile, M.; Basile, A. Chapter 1 - Methanol Production and Applications: An Overview. In *Methanol*, Basile, A.; Dalena, F.; Elsevier, 2018; pp. 3−28.

(10) Goeppert, A.; Czaun, M.; Jones, J.-P.; Surya Prakash, G. K.; Olah, G. A. Recycling of carbon dioxide to methanol and derived products − closing the loop. *Chem. Soc. Rev.* **2014**, *43* (23), 7995−8048.

(11) Chinchen, G. C.; Denny, P. J.; Jennings, J. R.; Spencer, M. S.; Waugh, K. C. Synthesis of Methanol: Part 1. Catalysts and Kinetics. *Appl. Catal.* **1988**, *36*, 1−65.

(12) Bozzano, G.; Manenti, F. Efficient methanol synthesis: Perspectives, technologies and optimization strategies. *Prog. Energy Combust. Sci* **2016**, *56*, 71−105.

(13) Saeidi, S.; Amin, N. A. S.; Rahimpour, M. R. Hydrogenation of CO_2 to value-added products—A review and potential future developments. *J. CO2 Util.* **2014**, *5*, 66−81.

(14) Aresta, M. *Carbon dioxide as chemical feedstock*; John Wiley & Sons, 2010.

(15) Li, C.; Yuan, X.; Fujimoto, K. Development of highly stable catalyst for methanol synthesis from carbon dioxide. *Appl. Catal., A* **2014**, *469*, 306−311.

(16) Niu, J.; Liu, H.; Jin, Y.; Fan, B.; Qi, W.; Ran, J. Comprehensive review of Cu-based CO_2 hydrogenation to CH_3OH: Insights from experimental work and theoretical analysis. *Int. J. Hydrogen Energy* **2022**, *47* (15), 9183−9200.

(17) Zhao, D.; Ortner, N.; Holena, M.; Wohlrab, S.; Kondratenko, E. V. Identifying Catalyst Property Descriptors for CO_2 Hydrogenation to Methanol via Big-Data Analysis. *ACS Catal.* **2023**, *13*, 10547−10559.

(18) Ortner, N.; Zhao, D.; Mena, H.; Weiß, J.; Lund, H.; Bartling, S.; Wohlrab, S.; Armbruster, U.; Kondratenko, E. V. Revealing Origins of Methanol Selectivity Loss in CO_2 Hydrogenation over CuZn-Containing Catalysts. *ACS Catal.* **2023**, *13* (1), 60−71.

(19) Behrens, M.; Studt, F.; Kasatkin, I.; Kühl, S.; Hävecker, M.; Abild-Pedersen, F.; Zander, S.; Girgsdies, F.; Kurr, P.; Kniep, B.-L.; Tovar, M.; Fischer, R. W.; Nørskov, J. K.; Schlögl, R. The Active Site of Methanol Synthesis over $Cu/ZnO/Al_2O_3$ Industrial Catalysts. *Science* **2012**, *336* (6083), 893−897.
(20) Pacchioni, G. From CO_2 to Methanol on $Cu/ZnO/Al_2O_3$ Industrial Catalyst. What Do We Know about the Active Phase and the Reaction Mechanism? *ACS Catal.* **2024**, *14* (4), 2730−2745.
(21) Bai, S.-T.; De Smet, G.; Liao, Y.; Sun, R.; Zhou, C.; Beller, M.; Maes, B. U. W.; Sels, B. F. Homogeneous and heterogeneous catalysts for hydrogenation of CO_2 to methanol under mild conditions. *Chem. Soc. Rev.* **2021**, *50* (7), 4259−4298.
(22) Zhao, D.; Han, S.; Kondratenko, E. V. CO_2 Hydrogenation to CH_3OH over Cu-Based Catalysts: Primary and Side Reactions. *ChemCatchem* **2023**, *15* (20), No. e202300679.
(23) Ren, S.; Fan, X.; Shang, Z.; Shoemaker, W. R.; Ma, L.; Wu, T.; Li, S.; Klinghoffer, N. B.; Yu, M.; Liang, X. Enhanced catalytic performance of Zr modified $CuO/ZnO/Al_2O_3$ catalyst for methanol and DME synthesis via CO_2 hydrogenation. *J. CO2 Util.* **2020**, *36*, 82−95.
(24) Dasireddy, V. D. B. C.; Štefančič, N. S.; Huš, M.; Likozar, B. Effect of alkaline earth metal oxide (MO) $Cu/MO/Al_2O_3$ catalysts on methanol synthesis activity and selectivity via CO_2 reduction. *Fuel* **2018**, *233*, 103−112.
(25) Xiao, J.; Mao, D.; Guo, X.; Yu, J. Effect of TiO_2, ZrO_2, and TiO_2−ZrO_2 on the performance of CuO−ZnO catalyst for CO_2 hydrogenation to methanol. *Appl. Surf. Sci.* **2015**, *338*, 146−153.
(26) Bonura, G.; Cordaro, M.; Cannilla, C.; Arena, F.; Frusteri, F. The changing nature of the active site of Cu-Zn-Zr catalysts for the CO_2 hydrogenation reaction to methanol. *Appl. Catal., B* **2014**, *152*−*153*, 152−161.
(27) Ladera, R.; Pérez-Alonso, F. J.; González-Carballo, J. M.; Ojeda, M.; Rojas, S.; Fierro, J. L. G. Catalytic valorization of CO_2 via methanol synthesis with Ga-promoted Cu−ZnO−ZrO_2 catalysts. *Appl. Catal., B* **2013**, *142*−*143*, 241−248.
(28) Porosoff, M. D.; Yan, B.; Chen, J. G. Catalytic reduction of CO_2 by H_2 for synthesis of CO, methanol and hydrocarbons: challenges and opportunities. *Energy Environ. Sci.* **2016**, *9* (1), 62−73.
(29) Melián-Cabrera, I.; López Granados, M.; Terreros, P.; Fierro, J. L. G. CO_2 hydrogenation over Pd-modified methanol synthesis catalysts. *Catal. Today* **1998**, *45* (1), 251−256.
(30) Choi, E. J.; Lee, Y. H.; Lee, D.-W.; Moon, D.-J.; Lee, K.-Y. Hydrogenation of CO_2 to methanol over Pd−Cu/CeO_2 catalysts. *Mol. Catal.* **2017**, *434*, 146−153.
(31) Hu, B.; Yin, Y.; Liu, G.; Chen, S.; Hong, X.; Tsang, S. C. E. Hydrogen spillover enabled active Cu sites for methanol synthesis from CO_2 hydrogenation over Pd doped CuZn catalysts. *J. Catal.* **2018**, *359*, 17−26.
(32) Jiang, X.; Nie, X.; Wang, X.; Wang, H.; Koizumi, N.; Chen, Y.; Guo, X.; Song, C. Origin of Pd-Cu bimetallic effect for synergetic promotion of methanol formation from CO_2 hydrogenation. *J. Catal.* **2019**, *369*, 21−32.
(33) Jiang, X.; Koizumi, N.; Guo, X.; Song, C. Bimetallic Pd−Cu catalysts for selective CO_2 hydrogenation to methanol. *Appl. Catal., B* **2015**, *170*−*171*, 173−185.
(34) Lee, K.; Anjum, U.; Araújo, T. P.; Mondelli, C.; He, Q.; Furukawa, S.; Pérez-Ramírez, J.; Kozlov, S. M.; Yan, N. Atomic Pd-promoted $ZnZrO_x$ solid solution catalyst for CO_2 hydrogenation to methanol. *Appl. Catal., B* **2022**, *304*, 120994.
(35) Huang, C.; Wu, Z.; Luo, H.; Zhang, S.; Shao, Z.; Wang, H.; Sun, Y. CO2 Hydrogenation to Methanol over PdZnZr Solid Solution: Effects of the PdZn Alloy and Oxygen Vacancy. *ACS Appl. Energy Mater.* **2021**, *4* (9), 9258−9266.
(36) Ojelade, O. A.; Zaman, S. F.; Daous, M. A.; Al-Zahrani, A. A.; Malik, A. S.; Driss, H.; Shterk, G.; Gascon, J. Optimizing Pd: Zn molar ratio in $PdZn/CeO_2$ for CO_2 hydrogenation to methanol. *Appl. Catal., A* **2019**, *584*, 117185.
(37) Fan, L.; Fujimoto, K. Development of an active and stable ceria-supported palladium catalyst for hydrogenation of carbon dioxide to methanol. *Appl. Catal., A* **1993**, *106* (1), L1−L7.
(38) Xu, J.; Su, X.; Liu, X.; Pan, X.; Pei, G.; Huang, Y.; Wang, X.; Zhang, T.; Geng, H. Methanol synthesis from CO_2 and H_2 over $Pd/ZnO/Al_2O_3$: Catalyst structure dependence of methanol selectivity. *Appl. Catal., A* **2016**, *514*, 51−59.
(39) Bahruji, H.; Esquius, J. R.; Bowker, M.; Hutchings, G.; Armstrong, R. D.; Jones, W. Solvent Free Synthesis of $PdZn/TiO_2$ Catalysts for the Hydrogenation of CO_2 to Methanol. *Topics Catal.* **2018**, *61* (3), 144−153.
(40) Zabilskiy, M.; Sushkevich, V. L.; Newton, M. A.; Krumeich, F.; Nachtegaal, M.; van Bokhoven, J. A. Mechanistic Study of Carbon Dioxide Hydrogenation over Pd/ZnO-Based Catalysts: The Role of Palladium−Zinc Alloy in Selective Methanol Synthesis. *Angew. Chem. Int. Ed.* **2021**, *60* (31), 17053−17059.
(41) Gentzen, M.; Doronkin, D. E.; Sheppard, T. L.; Zimina, A.; Li, H.; Jelic, J.; Studt, F.; Grunwaldt, J.-D.; Sauer, J.; Behrens, S. Supported Intermetallic PdZn Nanoparticles as Bifunctional Catalysts for the Direct Synthesis of Dimethyl Ether from CO-Rich Synthesis Gas. *Angew. Chem. Int. Ed.* **2019**, *58* (44), 15655−15659.
(42) Bahruji, H.; Bowker, M.; Hutchings, G.; Dimitratos, N.; Wells, P.; Gibson, E.; Jones, W.; Brookes, C.; Morgan, D.; Lalev, G. Pd/ZnO catalysts for direct CO_2 hydrogenation to methanol. *J. Catal.* **2016**, *343*, 133−146.
(43) Malik, A. S.; Zaman, S. F.; Al-Zahrani, A. A.; Daous, M. A.; Driss, H.; Petrov, L. A. Development of highly selective $PdZn/CeO_2$ and Ca-doped $PdZn/CeO_2$ catalysts for methanol synthesis from CO_2 hydrogenation. *Appl. Catal., A* **2018**, *560*, 42−53.
(44) Kunkes, E. L.; Studt, F.; Abild-Pedersen, F.; Schlögl, R.; Behrens, M. Hydrogenation of CO_2 to methanol and CO on $Cu/ZnO/Al_2O_3$: Is there a common intermediate or not? *J. Catal.* **2015**, *328*, 43−48.
(45) Ravel, B.; Newville, M. ATHENA, ARTEMIS, HEPHAESTUS: data analysis for X-ray absorption spectroscopy using IFEFFIT. *J. Synchrotron Rad.* **2005**, *12* (4), 537−541.
(46) Tan, H.; Wang, J.; Yu, S.; Zhou, K. Support Morphology-Dependent Catalytic Activity of Pd/CeO_2 for Formaldehyde Oxidation. *Environ. Sci. Technol.* **2015**, *49* (14), 8675−8682.
(47) Gao, P.; Xie, R.; Wang, H.; Zhong, L.; Xia, L.; Zhang, Z.; Wei, W.; Sun, Y. Cu/Zn/Al/Zr catalysts via phase-pure hydrotalcite-like compounds for methanol synthesis from carbon dioxide. *J. CO2 Util.* **2015**, *11*, 41−48.
(48) Jiang, X.; Nie, X.; Guo, X.; Song, C.; Chen, J. G. Recent Advances in Carbon Dioxide Hydrogenation to Methanol via Heterogeneous Catalysis. *Chem. Rev.* **2020**, *120* (15), 7984−8034.
(49) Du, Y.-P.; Bahmanpour, A. M.; Milošević, L.; Héroguel, F.; Mensi, M. D.; Kröcher, O.; Luterbacher, J. S. Engineering the ZrO_2−Pd Interface for Selective CO_2 Hydrogenation by Overcoating an Atomically Dispersed Pd Precatalyst. *ACS Catal.* **2020**, *10* (20), 12058−12070.
(50) Shen, W.-J.; Okumura, M.; Matsumura, Y.; Haruta, M. The influence of the support on the activity and selectivity of Pd in CO hydrogenation. *Appl. Catal., A* **2001**, *213* (2), 225−232.
(51) Zhang, Z.; Zhang, L.; Hülsey, M. J.; Yan, N. Zirconia phase effect in Pd/ZrO_2 catalyzed CO_2 hydrogenation into formate. *Mol. Catal.* **2019**, *475*, 110461.
(52) Li, Q.; Wang, Y.; Si, W.; Peng, Y.; Li, J. Novel Insights on the Metal−Support Interactions of Pd/ZrO_2 Catalysts on CH_4 Oxidation. *ACS Appl. Mater. Interf.* **2023**, *15* (6), 7959−7968.
(53) Zhang, J.; Gao, Y.; Jia, X.; Wang, J.; Chen, Z.; Xu, Y. Oxygen vacancy-rich mesoporous ZrO_2 with remarkably enhanced visible-light photocatalytic performance. *Sol. Energy Mater.* **2018**, *182*, 113−120.
(54) Tabata, K.; Hirano, Y.; Suzuki, E. XPS studies on the oxygen species of $LaMn_{1-x}Cu_xO_{3+\lambda}$. *Appl. Catal., A* **1998**, *170* (2), 245−254.
(55) Idriss, H. On the wrong assignment of the XPS O1s signal at 531−532 eV attributed to oxygen vacancies in photo- and electro-catalysts for water splitting and other materials applications. *Surf. Sci.* **2021**, *712*, 121894.

https://doi.org/10.1021/acscatal.4c07462
ACS Catal. 2025, 15, 2328−2341

(56) Luo, Z.; Tian, S.; Wang, Z. Enhanced Activity of Cu/ZnO/C Catalysts Prepared by Cold Plasma for CO_2 Hydrogenation to Methanol. *Ind. Eng. Chem. Res.* **2020**, *59* (13), 5657−5663.
(57) Marcos, F. C. F.; Lin, L.; Betancourt, L. E.; Senanayake, S. D.; Rodriguez, J. A.; Assaf, J. M.; Giudici, R.; Assaf, E. M. Insights into the methanol synthesis mechanism via CO_2 hydrogenation over Cu-ZnO-ZrO_2 catalysts: Effects of surfactant/Cu-Zn-Zr molar ratio. *J. CO_2 Util.* **2020**, *41*, 101215.
(58) Gentzen, M.; Doronkin, D. E.; Sheppard, T. L.; Grunwaldt, J. D.; Sauer, J.; Behrens, S. Bifunctional catalysts based on colloidal Cu/Zn nanoparticles for the direct conversion of synthesis gas to dimethyl ether and hydrocarbons. *Appl. Catal., A* **2018**, *557*, 99−107.
(59) Jia, X.; Zhang, X.; Rui, N.; Hu, X.; Liu, C.-J. Structural effect of Ni/ZrO_2 catalyst on CO_2 methanation with enhanced activity. *Appl. Catal., B* **2019**, *244*, 159−169.
(60) Köck, E.-M.; Kogler, M.; Bielz, T.; Klötzer, B.; Penner, S. In Situ FT-IR Spectroscopic Study of CO_2 and CO Adsorption on Y_2O_3, ZrO_2, and Yttria-Stabilized ZrO_2. *J. Phys. Chem. C* **2013**, *117* (34), 17666−17673.
(61) Pokrovski, K.; Jung, K. T.; Bell, A. T. Investigation of CO and CO_2 Adsorption on Tetragonal and Monoclinic Zirconia. *Langmuir* **2001**, *17* (14), 4297−4303.
(62) Hill, I. M.; Hanspal, S.; Young, Z. D.; Davis, R. J. DRIFTS of probe molecules adsorbed on magnesia, Zirconia, and hydroxyapatite catalysts. *J. Phys. Chem. C* **2015**, *119* (17), 9186−9197.
(63) Wang, Y.; Kattel, S.; Gao, W.; Li, K.; Liu, P.; Chen, J. G.; Wang, H. Exploring the ternary interactions in Cu−ZnO−ZrO_2 catalysts for efficient CO_2 hydrogenation to methanol. *Nat. Commun.* **2019**, *10* (1), 1166.
(64) Wang, J.; Li, G.; Li, Z.; Tang, C.; Feng, Z.; An, H.; Liu, H.; Liu, T.; Li, C. A highly selective and stable ZnO-ZrO_2 solid solution catalyst for CO_2 hydrogenation to methanol. *Sci. Adv.* **2017**, *3* (10), No. e1701290.
(65) Bianchi, D.; Chafik, T.; Khalfallah, M.; Teichner, S. J. Intermediate species on zirconia supported methanol aerogel catalysts. *Appl. Catal. A Gen.* **1993**, *105* (2), 223−249.
(66) Kattel, S.; Yan, B.; Yang, Y.; Chen, J. G.; Liu, P. Optimizing binding energies of key intermediates for CO_2 hydrogenation to methanol over oxide-supported copper. *J. Am. Chem. Soc.* **2016**, *138* (38), 12440−12450.
(67) Yang, M.; Yu, J.; Zimina, A.; Sarma, B. B.; Pandit, L.; Grunwaldt, J.-D.; Zhang, L.; Xu, H.; Sun, J. Probing the Nature of Zinc in Copper-Zinc-Zirconium Catalysts by Operando Spectroscopies for CO_2 Hydrogenation to Methanol. *Angew. Chem. Int. Ed.* **2023**, *62* (7), No. e202216803.
(68) Simonovis, J. P.; Zhang, H.; Rui, N.; Hunt, A.; Orozco, I.; Liu, P.; Senanayake, S. D.; Rodriguez, J. A.; Waluyo, I. Investigating the Elusive Nature of Atomic O from CO_2 Dissociation on Pd(111): The Role of Surface Hydrogen. *J. Phys. Chem. C* **2022**, *126* (18), 7870−7879.
(69) Tereshchenko, A.; Guda, A.; Polyakov, V.; Rusalev, Y.; Butova, V.; Soldatov, A. Pd nanoparticle growth monitored by DRIFT spectroscopy of adsorbed CO. *Analyst* **2020**, *145* (23), 7534−7540.
(70) Ebbesen, S. D.; Mojet, B. L.; Lefferts, L. The influence of water and pH on adsorption and oxidation of CO on Pd/Al_2O_3 - an investigation by attenuated total reflection infrared spectroscopy. *Phys. Chem. Chem. Phys.* **2009**, *11* (4), 641−649.
(71) Szanyi, J.; Kuhn, W. K.; Goodman, D. W. CO adsorption on Pd(111) and Pd(100): Low and high pressure correlations. *J. Vac. Sci. Technol., A* **1993**, *11* (4), 1969−1974.
(72) Jiang, X.; Wang, X.; Nie, X.; Koizumi, N.; Guo, X.; Song, C. CO_2 hydrogenation to methanol on Pd-Cu bimetallic catalysts: H_2/CO_2 ratio dependence and surface species. *Catal. Today* **2018**, *316*, 62−70.
(73) Manrique, R.; Rodríguez-Pereira, J.; Rincón-Ortiz, S. A.; Bravo-Suárez, J. J.; Baldovino-Medrano, V. G.; Jiménez, R.; Karelovic, A. The nature of the active sites of Pd−Ga catalysts in the hydrogenation of CO_2 to methanol. *Catal. Sci. Technol.* **2020**, *10* (19), 6644−6658.
(74) Gallagher, J. R.; Childers, D. J.; Zhao, H.; Winans, R. E.; Meyer, R. J.; Miller, J. T. Structural evolution of an intermetallic Pd-Zn catalyst selective for propane dehydrogenation. *Phys. Chem. Chem. Phys.* **2015**, *17* (42), 28144−28153.
(75) Stakheev, A. Y.; Smirnova, N. S.; Krivoruchenko, D. S.; Baeva, G. N.; Mashkovsky, I. S.; Yakushev, I. A.; Vargaftik, M. N. Single-atom Pd sites on the surface of Pd−In nanoparticles supported on γ-Al_2O_3: a CO-DRIFTS study. *Mendeleev Commun.* **2017**, *27* (5), 515−517.
(76) Knell, A.; Barnickel, P.; Baiker, A.; Wokaun, A. CO oxidation over Au/ZrO_2 catalysts: Activity, deactivation behavior, and reaction mechanism. *J. Catal.* **1992**, *137* (2), 306−321.
(77) Zhou, W.; Ma, Z.; Guo, S.; Wang, M.; Wang, J.; Xia, M.; Jia, L.; Hou, B.; Li, D.; Zhao, Y. Comparative study of CO adsorption on zirconia polymorphs with DRIFT and transmission FT-IR spectroscopy. *Appl. Surf. Sci.* **2018**, *427*, 867−873.
(78) Fedorova, E. A.; Kraußer, L.; Weiß, J.; Fedorov, A.; Brückner, A.; Kondratenko, E. V.; Kubis, C. Operando DRIFTS Investigations on Surface Intermediates and Effects of Potassium in CO_2 Hydrogenation over a K−Fe/$YZrO_x$ Catalyst. *ChemCatchem* **2024**, *16* (10), No. e202301697.
(79) Wang, Y.; Gao, W.; Li, K.; Zheng, Y.; Xie, Z.; Na, W.; Chen, J. G.; Wang, H. Strong Evidence of the Role of H_2O in Affecting Methanol Selectivity from CO_2 Hydrogenation over Cu-ZnO-ZrO_2. *Chem* **2020**, *6* (2), 419−430.
(80) Yang, Y.; White, M. G.; Liu, P. Theoretical Study of Methanol Synthesis from CO_2 Hydrogenation on Metal-Doped Cu(111) Surfaces. *J. Phys. Chem. C* **2012**, *116* (1), 248−256.

https://doi.org/10.1021/acscatal.4c07462
ACS Catal. 2025, 15, 2328−2341